

Understanding of Catalytic ROS Generation From Defect-Rich Graphene Quantum-Dots for Therapeutic Effects in Tumor Microenvironment

Xichu Wang

University of New South Wales - Kensington Campus: University of New South Wales

Chuangang Hu

University of New South Wales - Kensington Campus: University of New South Wales

Zi (Sophia) Gu (✉ zi.gu1@unsw.edu.au)

University of New South Wales <https://orcid.org/0000-0002-7153-6596>

Liming Dai

University of New South Wales - Kensington Campus: University of New South Wales

Research

Keywords: carbon-based metal-free catalyst, graphene quantum dot, defect, reactive oxygen species, tumor microenvironment.

Posted Date: July 8th, 2021

DOI: <https://doi.org/10.21203/rs.3.rs-657051/v1>

License:  This work is licensed under a Creative Commons Attribution 4.0 International License.

[Read Full License](#)

Understanding of catalytic ROS generation from defect-rich graphene quantum-dots for therapeutic effects in tumor microenvironment

Xichu Wang¹, Chuangang Hu¹, Zi Gu^{1,*}, Liming Dai^{1,*}

¹ *Australian Carbon Materials Centre (A-CMC), School of Chemical Engineering, University of New South Wales, Sydney, NSW 2052, Australia.*

**Joint senior authors, to whom correspondence should be addressed. Emails:*
zi.gu1@unsw.edu.au (Dr. Zi Gu), l.dai@unsw.edu.au (Prof. Liming Dai)

Keywords: carbon-based metal-free catalyst, graphene quantum dot, defect, reactive oxygen species, tumor microenvironment.

Abstract

Owing to their low cost, high catalytic efficiency and biocompatibility, carbon-based metal-free catalysts (C-MFCs) have attracted intense interest for various applications, ranging from energy through environmental to biomedical technologies. While considerable efforts and progress have been made in mechanistic understanding of C-MFCs for non-biomedical applications, their catalytic mechanism for therapeutic effects has rarely been investigated. In this study, defect-rich graphene quantum dots (GQDs) were developed as C-MFCs for efficient ROS generation, specifically in the H₂O₂-rich tumor microenvironment to cause multi-level damage of subcellular components (even in nuclei). While a desirable anti-cancer performance was achieved, the catalytic performance was found to strongly depend on the defect density. It is for the first time that the defect-induced catalytic generation of ROS by C-MFCs in the tumor microenvironment was demonstrated and the associated catalytic mechanism was elucidated. This work opens a new avenue for the development of safe and efficient catalytic nanomedicine.

Background

Reactive Oxygen species (ROS) play an important role in maintaining biological functions. Cells inherently produce ROS that serves as cell signaling molecules for normal biological processes¹. On the other hand, excessive ROS could induce oxidative stress to damage lipids, proteins and DNA, leading to apoptosis¹⁻⁴, necroptosis², and autophagic cell death^{3,5}. Thus, ROS-induced cell death could be one of the attractive options for cancer therapy if the cancer cell-specific ROS generation can be achieved. Nevertheless, the tumor microenvironment (TME) is a unique protective ecosystem that helps cancer cells to thrive⁶, and a high level of hydrogen peroxide in TME has been demonstrated to promote tumor growth through apoptosis resistance, DNA alteration, cell proliferation angiogenesis⁷. In the presence of an appropriate catalyst, hydrogen peroxide can be used for the catalytic generation of ROS, which, if excessively generated in a TME, could be used to kill cancer cells. Therefore, the catalyst is a key for ROS-induced cancer cell death.

By making redox reaction catalysts respond to specific biological milieu to achieve therapeutic effects, catalytic nanomaterials hold great promise to harness redox reactions for biochemical applications. In this context, catalytic nanomaterials have been used to mediate reactions to convert non-therapeutic compounds in the tumor environment to therapeutic agents for specifically killing tumor cells. In particular, iron nanoparticles^{8,9} were used to disproportionate H₂O₂ in the tumor microenvironment to cytotoxic hydroxyl radicals (·OH) via Fenton(-like) reactions. Other nanoparticles, containing Mn, Co, Cu, or Ag element^{6,10-13}, have also been demonstrated to act as nanozyme agents for inhibiting tumor growth. However, metal-containing nanoparticles with a strong chelation ability could interfere with the functionalities of biological molecules and/or tissues to inevitably expose biosafety risks⁵. By contrast, metal-free carbon-based catalysts (C-MFCs) are biocompatible, cost-effective, and multifunctional¹⁴.

Since the discovery of nitrogen (N)-doped carbon nanotube catalyst as the first C-MFC for electrocatalytic oxygen reduction reaction (ORR) in 2009¹⁵, C-MFCs have been widely explored as efficient, low-cost alternatives to metal-based catalysts for energy, environmental and biomedical applications¹⁶. Of particular interest, N-doped carbon nanospheres have recently been investigated as nanozymes for catalytic cancer treatments by producing hydroxyl radicals from H₂O₂¹⁷. In this particular case, N-doping was attributed to being responsible for the generation of hydroxyl radicals. N-doping has been previously revealed to cause charge redistribution around adjacent carbon atoms to induce the catalytic activities¹⁸. Similarly, defects in carbon nanomaterials could also alter charge distributions to induce catalytic performance¹⁹⁻²⁰, which has been confirmed by recent experimental and theoretical studies for energy-related reactions (e.g., ORR)¹⁸⁻²¹. So far, however, there is no study on the mechanistic understanding of defect-induced biocatalytic behaviors.

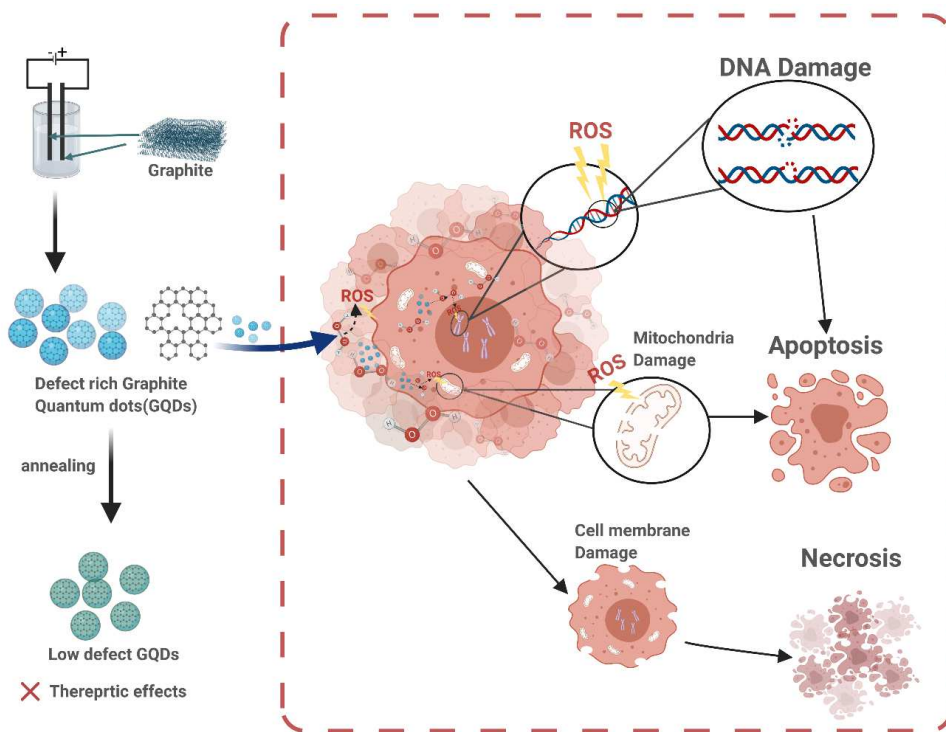


Fig. 1: Schematic illustration of synthetic procedure and multi-target therapeutic mechanism of graphene quantum dots (GQDs). Figure created with BioRender.

Owing to their small size, unique physicochemical properties, and biocatalytic behaviors, graphene quantum dots (GQDs) have been investigated as promising C-MFC-based therapeutic agents²². Recent studies demonstrated that graphene quantum dots functionalized with and without targeting agent (s) can cause DNA damage via ROS generation to suppress the growth of cancer cells²³⁻²⁴. However, underlying mechanisms for the GQD-induced ROS generation have not yet been understood, though the associated ROS-induced DNA damage and biochemical anti-cancer effect have been widely studied. In this work, we have for the first time demonstrated the defect-induced ROS generation from GQD C-MFCs and hydrogen peroxide in TME and carried out the associated mechanistic study.

Herein, metal-free, doping-free, defect-rich GQDs were used to study the defect-induced catalytic generation of hydroxyl radicals ($\cdot\text{OH}$) and the subsequent biological effects. Spin-trapped electron paramagnetic resonance (EPR) spectroscopy and colorimetric assay studies revealed that the catalytic performance strongly depends on the defect density. As schematically shown in Fig. 1, defect-rich GQDs could catalyze the efficient generation of hydroxyl radicals from hydrogen peroxide, especially in TME, to induce an efficacious anti-cancer effect even without the addition of any chemotherapeutic drugs. Our cellular and subcellular studies revealed multi-level anti-cancer mechanisms involving the cell membrane, mitochondria, and DNA damages by the defect-rich GQDs (Fig. 1). This newly observed GQD defect-induced catalytic ROS generation, along with the associated therapeutic effects in response to TME, represents the first proof of concept for the defect-induced metal-free catalytic therapeutic strategy towards safe and efficacious cancer treatment.

Results and discussion

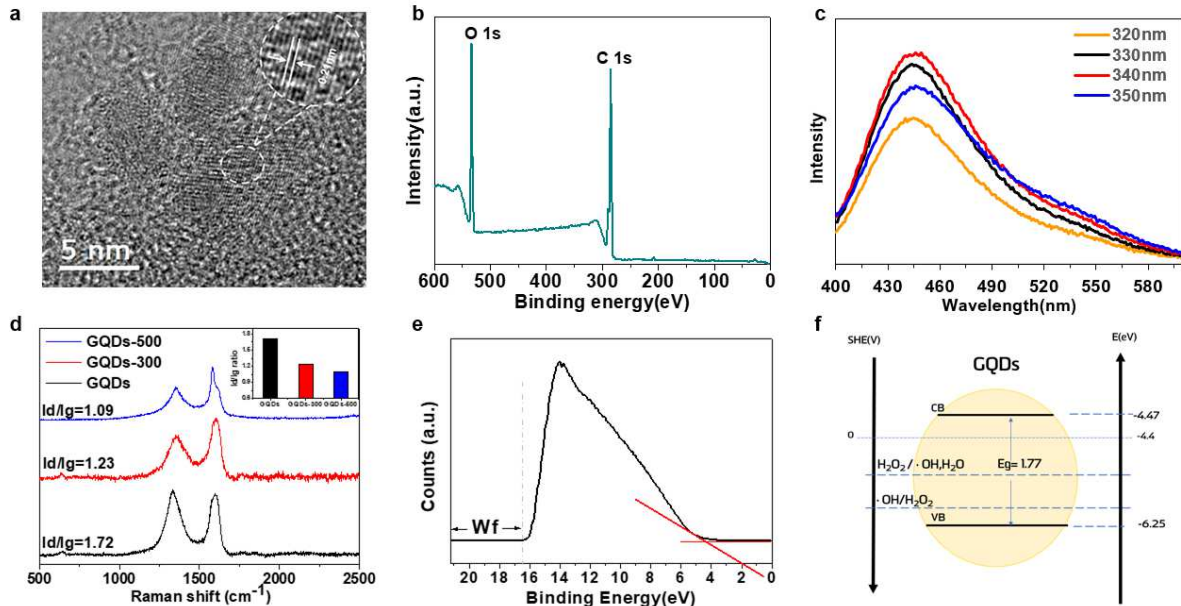


Fig. 2: Physicochemical properties of GQDs. **a** TEM image (scale bar = 5 nm). **b** XPS survey spectra (insert: HR-XPS spectra of C1s). **c** Fluorescence emission spectrum at the excitation wavelength of different wavelengths ranging from 320 nm to 350 nm. **d** Raman spectra of GQDs with different defect densities (insert: Id/Ig ratio of GQDs with different defect densities). **e** UPS spectra of GQDs. **f** Band structure of GQDs. Conduction band(CV) = Valence band(VB) + E_g^{opt25} .

Synthesis and structural characterization of GQDs

The GQDs used in this study were synthesized and purified via a typical electrochemical method without further modification, according to a published procedure²⁶. GQDs-300 and GQDs-500 were obtained by annealing the purified GQDs at 300 °C and 500 °C, respectively. The high-resolution transmission electron microscopic (HRTEM) examination revealed a spherical morphology with an average diameter of about 3.5 nm and crystal lattice spacing of 0.22 nm for the GQDs (Fig. 2a). The aqueous dispersion of GQDs was relatively stable at room

temperature, which showed an average hydrodynamic particle size of 9.8 nm and zeta potential of -22.5mV with no change over 30 days (Supplementary Fig.S1&S2).

To investigate the chemical compositions of the GQDs, we performed X-ray photoelectron spectroscopy (XPS) and Fourier-transform infrared spectroscopy (FT-IR). XPS analyses indicate the presence of C (72 at%) and O (26 at%) in GQDs (Fig. 2b). The corresponding ultraviolet-visible (UV-vis) absorption spectrum of the aqueous dispersion of GQDs shows a typical broad absorption peak at 230 nm attributable to $\pi = \pi^*$ transition of the aromatic C=O bond²⁷ (Supplementary Fig.S4). Fig. 2c shows photoluminescent emissions at different excitation wavelengths (from 350 nm to 800 nm) for an aqueous dispersion of GQDs, indicating the highest emission peak at 450 nm under excitation at 340 nm (Fig. 2c). Fig. 2d reproduces the Raman spectrum for the GQDs, which shows the presence of the crystalline G band (1596 cm^{-1}) and disordered D band (1331 cm^{-1}) with an I_D/I_G ratio of 1.72, indicating a defect-rich structure²⁸.

For comparison, GQDs with relatively low defect densities were also synthesized via annealing under an argon atmosphere at $300\text{ }^\circ\text{C}$ (GQDs-300) and $500\text{ }^\circ\text{C}$ (GQDs-500), as mentioned above. As expected, annealing at higher temperatures could effectively reduce the defect density, as demonstrated by the decreased I_D/I_G ratios in the order of 1.72, 1.23 and 1.09 for the pristine GQDs, GQDs-300, and GQDs-500, respectively (Fig. 2d).

Fig. 2f shows the band structure diagram for the GQDs, which was obtained from the corresponding optical energy gap, deduced from the longest absorption edge ($\lambda_{onset}, E_g^{\text{opt}} = 1.77\text{ eV}$)²⁹, and the highest occupied molecular orbital (HOMO) at the valence band from UPS (6.25 eV, Fig. 2e). The lowest unoccupied molecular orbital (LUMO) at the conduction band was then calculated to be: $E_g^{\text{opt}} - \text{HOMO} = 1.77 - 6.25 = -4.47$ (Fig. 2f, Supplementary

Table S1). Based on the calculated band structure and redox potentials shown in Fig. 2f, the GQDs-defect catalyzed hydroxyl radical generation from H₂O₂ is plausible.

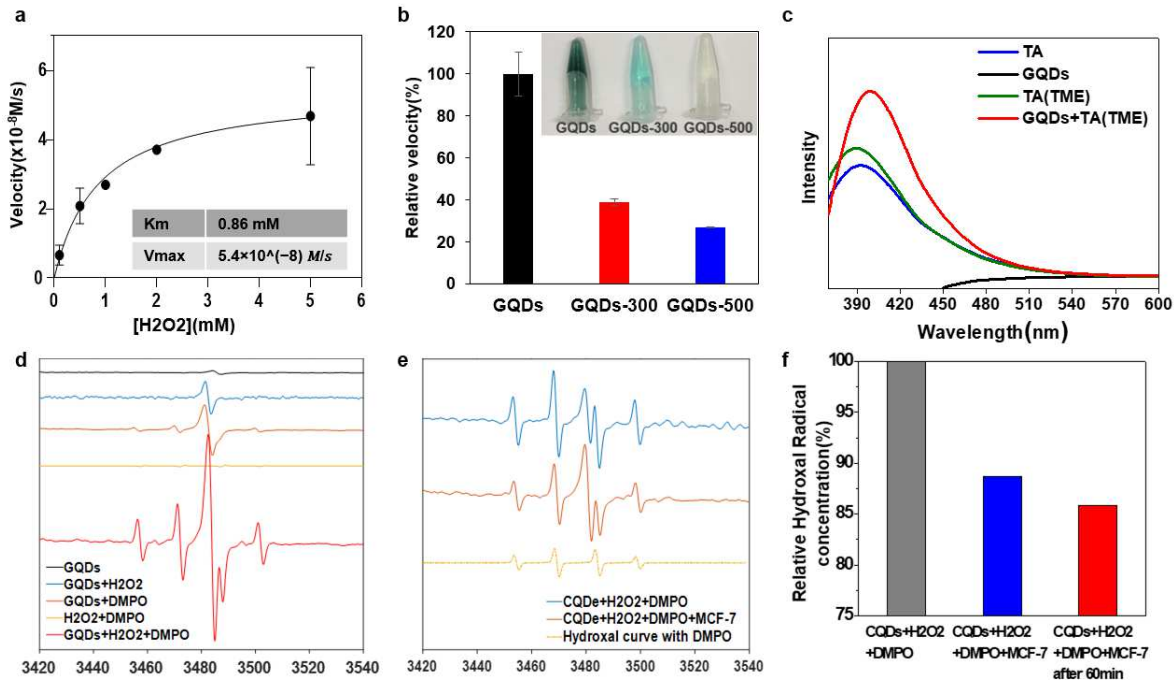


Fig. 3: Catalytic performance of GQDs. **a** Michaelis-Menten kinetic profile. **b** Catalytic performance comparison via relative reaction velocity from TMB assay (in Hac/NaAc buffer) for GQDs (100 µg/ml) with different treatments (untreated, GQDs-300, GQDs-500) under TME(100 µM H₂O₂), insert: photo of TMB color assay at 10 min post-treatment of GQDs, GQDs-300, GQDs-500. **c** Fluorescence spectra of TA, GQDs, TA (TME) and GQDs+TA (TME) in PBS. The concentration of TA, TME (H₂O₂) and GQDs in PBS were 1 mM, 100 µM and 100 µg/ml, respectively. Hydroxyl radical identification via EPR using DMPO (1 mM) as the spin trap of: **d** GQDs (50 µg/ml) with and without H₂O₂ (1 mM), and **e** GQDs+H₂O₂ with and without adding MCF-7 cells (1×10^6 /ml). **f** Relative hydroxyl radical concentrations calculated from the signals in using Xenon quantify EPR software.

Defect-induced catalytic activity. We found that defect-rich GQDs possess a peroxidase-like activity that decomposes hydrogen peroxide (H₂O₂) into hydroxyl radicals (·OH). To test the

catalytic performance of the GQDs, we used the 3,3,5,5-tetramethylbenzidine (TMB) assay, which can be oxidized by ·OH from H₂O₂ decomposition to a blue product with absorbance at 652 nm³⁰. As shown in Supplementary Fig. S6&S7, GQDs significantly increased the reaction rates of H₂O₂ decomposition, followed by · OH induced TMB oxidation. By plotting initial velocities against H₂O₂ concentrations, we performed the kinetic analysis and calculated the Michaelis-Menten constant (K_m) and maximum initial velocity (V_{max})¹⁷ to be 0.86 mM and 5.4×10⁻⁸ M/s, respectively (Fig. 3a & Supplementary Fig.S5&S7), indicating the high catalytic activity of GQDs⁸. We further used TMB and GQDs of different defect densities to investigate the effect of defect density on catalytic activity. As shown in Fig. 3b, the reaction velocity of GQDs (control, as 100%) decreased dramatically to 39% for GQDs-300 and 26% for GQDs-500, suggesting that a high defect density is critical to the enhanced catalytic activity.

To gain a mechanistic understanding of catalytic ROS generation, we used terephthalic acid (TA) as a specific hydroxyl radical probe to capture hydroxyl radicals for the generation of 2-hydroxyl terephthalic acid (TAOH) with fluorescence emission at 400 nm³¹⁻³². The fluorescent intensity from a mixed solution of GQDs, H₂O₂ and TA significantly increased in comparison to the control solutions of TA, H₂O₂+TA, and GQDs+TA, signifying the generation of abundant ·OH radicals from the interaction between GQDs and H₂O₂ (Fig. 3c & Supplementary Figs S8&S9). This result suggests that GQDs possess the catalytic ability toward H₂O₂ decomposition to generate ·OH. The catalytic nature of GQDs was further supported by the same chemical structure before and after the reaction, demonstrated by FT-IR spectra of GQDs (Supplementary Fig. S3).

In vitro ROS regulation and the associated biological effects in TME. As can be seen from the above discussion, the defect-rich GQDs can induce peroxidase-like catalytic reactions to decompose H₂O₂ into ·OH. To confirm this, we firstly used electron paramagnetic resonance (EPR) spectroscopy, in conjunction with 5,5-dimethyl-1-pyrroline N-oxide (DMPO) as a

typical nitrone spin trap, to identify ·OH species³³. As shown in Fig. 3d, EPR spectra reveal a characteristic 1:2:2:1 signal pattern of ·OH in the sample containing both H₂O₂ and GQDs, but not in the samples without GQDs or H₂O₂. These results confirm that the GQDs can catalyze H₂O₂ decomposition to generate ·OH (Fig. 3d and Supplementary Fig.S10). To study the effect of hydroxyl radicals on cultured cancer cells, we incubated $1 \times 10^6/\text{ml}$ MCF-7 cells in a mixture of H₂O₂ and GQDs (50 µg/ml) for 60 min. Aliquots collected from the fresh mixture and after 60 min were evaluated by EPR using the DMPO nitrone spin trap. As shown in Fig. 3e&f, MCF-7 cancer cells continuously consumed ·OH generated from the CQDs catalyzed H₂O₂ decomposition.

To investigate the subcellular accumulation of GQDs, we performed the intracellular mapping of GQDs in human breast cancer MCF-7 cell culture by using dyes Dil and NucRed647 for visualizing plasma membrane and nuclei, respectively. As shown in confocal microscopy images given in Fig. 4a&b (Supplementary, movie3&4), the GQDs with blue fluorescence emission under 405-nm excitation were found in both cytoplasm and nuclei in an aggregated form. The driving force for GQDs to penetrate the cell and accumulate in nuclei probably arises from both the size effect and the π–π stacking interactions between GQDs and DNA chains²³.

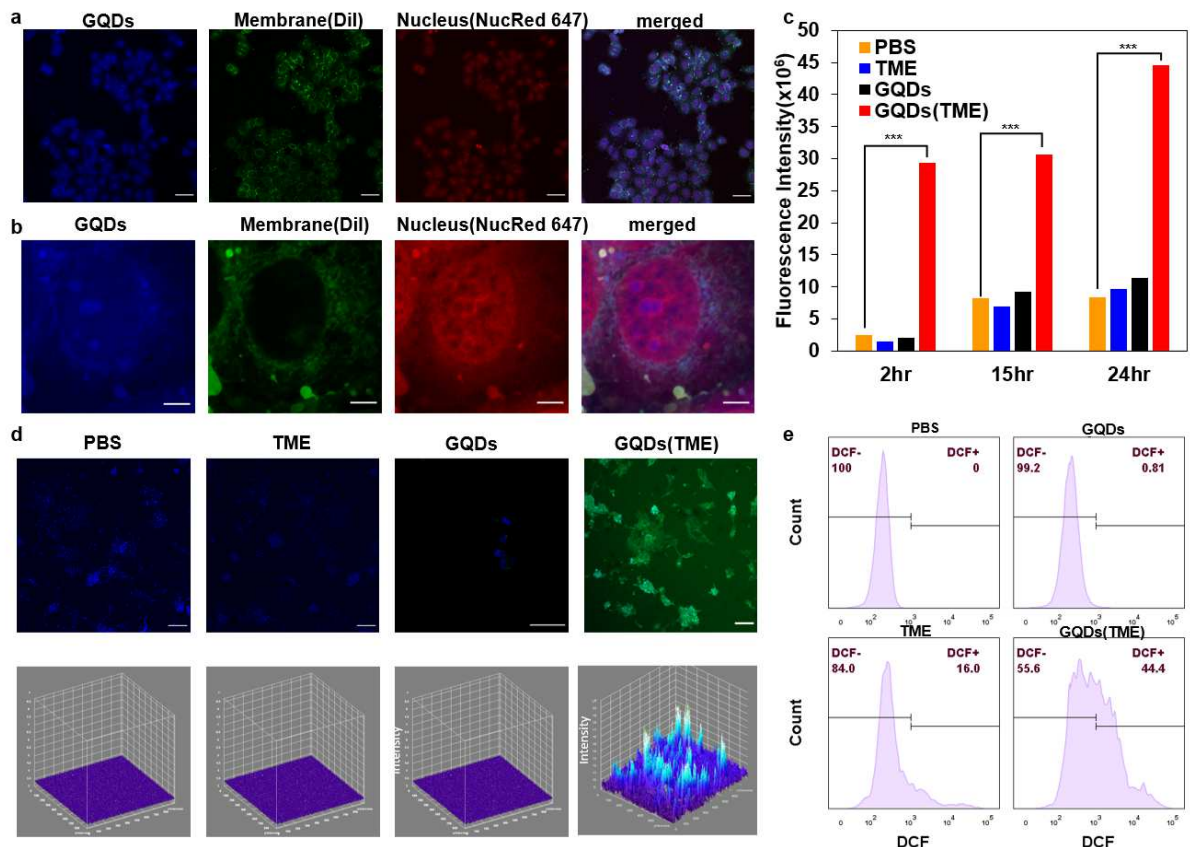


Fig. 4: Cellular localization of GQDs and intracellular ROS generation. **a, b** Fluorescence microscopy images of GQDs-treated MCF-7 cells (**a**: scale bar: 50 μ M, **b**: scale bar: 10 μ M). **c** Fluorescence intensity of DCF in 4T1 cell lines at 2, 15 and 24 hr post-treatment of PBS, GQDs (100 μ g/ml), TME (100 μ M H₂O₂), GQD (TME) (100 μ g/ml GQDs + 100 μ M H₂O₂). **d** intracellular ROS level in 4T1 cells (green signals from DCF indicate ROS; blue signals from DAPI indicate nuclei), scale bar: 100 μ m. **e** Quantified intracellular ROS level in 4T1 cells treated with agents: PBS, GQDs (100 μ g/ml), TME (100 μ M H₂O₂), GQD (TME) (100 μ g/ml GQDs + 100 μ M H₂O₂) for 2 h, measured by flow cytometry. Data are presented as mean \pm standard deviation, and analyzed by unpaired Student's two-tailed t-test, compared to PBS group. *p<0.05, **p<0.01, ***p<0.001.

Hydrogen peroxide overexpression is a well-known hallmark of cancers, which can show a 10-fold increase compared to normal cells⁷. Thus, the above-demonstrated catalytic capability of

GQDs can be exploited to decompose H₂O₂ into cytotoxic ·OH radicals to efficiently kill cancer cells, particularly in the tumor microenvironment. In this study, we used DCFH-DA as a fluorescence probe to evaluate the intracellular radical generation in response to GQDs in the tumor microenvironment. It is known that DCFH-DA can permeate into cells and be intracellularly hydrolyzed to DCFH, then further oxidized by intracellular ROS to fluorescent product dichlorofluorescein (DCF)³⁴. The time-dependent, TME-responsive, GQDs-induced ROS generation was demonstrated by DCF fluorescence intensities recorded on a photoluminescent spectrometer at 2, 15, and 24 h after the addition of GQDs. Fig. 4c shows a burst production of ROS within the first 2-h treatment of GQDs in the tumor microenvironment, followed by a continued increase in the intracellular ROS level over 24 h. In contrast, a retarded low-level ROS generation was observed in control experiments without GQDs or TME (Fig. 4c). The intracellular ROS levels were also visualized by confocal microscopy (Fig. 4d). As expected, significant fluorescence emissions from DCF were observed in the treatment group of GQDs in TME, rather than in the control groups (i.e. PBS, TME, GQDs). The intracellular level of ROS was further quantified via flow cytometry, which demonstrated 0.81 %, 16 % and 44.4 % of fluorescent cells for the GQDs, TME, and GQDs (TME), respectively (Fig. 4e), confirming, once again, that the defect-rich GQDs can catalyze the generation of a considerable amount of ROS in the tumor microenvironment.

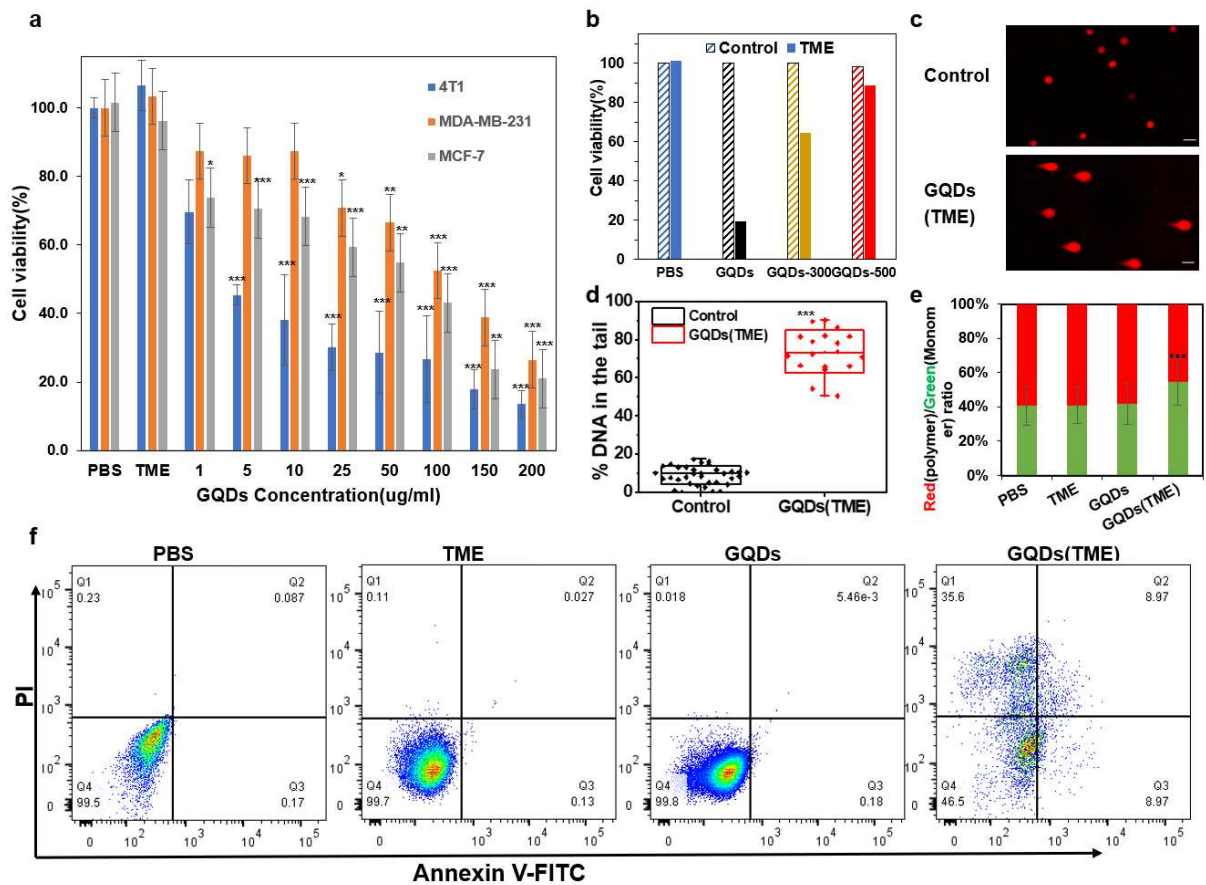


Fig. 5: Therapeutic effects of GQD under TME. **a** Cell viability of 4T1/MDA-MB-231/MCF-7 cells treated with PBS, 100 μM H_2O_2 (TME), or GQDs (1-200 $\mu\text{g}/\text{ml}$) + 100 μM H_2O_2 under TME, for 24 h. **b** Cell viability of 4T1 cells treated with PBS, GQDs, GQDs-300 or GQDs-500 for 24h. **c** Neutral comet assay of GQDs (200 $\mu\text{g}/\text{ml}$) under TME. **d** quantitative analysis of alkaline comet assay based on 30 cell samples. **e** The ratio of red (JC-1 polymer) over green (JC-1 monomer) fluorescence intensity of different treatment groups including PBS, TME, 100 $\mu\text{g}/\text{ml}$ GQDs, and GQDs(1-100 $\mu\text{g}/\text{ml}$) + 100 μM H_2O_2 , representing the changes in mitochondria membrane potential. **f** apoptosis analysis via flow cytometry. Data are presented as mean \pm SD. Statistical significance was analyzed by unpaired Student's two-tailed t-test compared to the PBS group. * $p<0.05$, ** $p<0.01$, *** $p<0.001$.

To evaluate the biologic effects of GQDs-mediated catalytic ROS generation, we measured the cell viability of breast cancer cells (4T1, MDA-MB-231, MCF-7) via CCK-8 assay by incubating three types of cell lines with GQDs at various concentrations under the TME-mimic conditions ($100 \mu\text{M H}_2\text{O}_2$)³⁵. It is interesting to note that the addition of low-concentration hydrogen peroxide (below $100 \mu\text{M}$) caused a slight increase in the cell viability of 4T1 (Supplementary Fig. S11), attributable to the fact that hydrogen peroxide could activate cancer cell growth by promoting cell malignant transformation and expression of H_2O_2 -detoxifying compounds⁷. As shown in Fig. 5a, a GQDs concentration-specific and TME-selective cell viability was observed under TME conditions. Specifically, in 4T1 cell cultures, GQDs under TME achieved 80% inhibition on cell viability at $200 \mu\text{g/ml}$ GQDs, with a half maximum inhibitory concentration (IC₅₀) of $50 \mu\text{g/ml}$ (Fig. 5a). When the GQD concentration increased from 1 to $200 \mu\text{g/ml}$, cell viability decreased from 70 to 20%. Similarly, defect-rich GQDs exhibited dosage-dependent cytotoxicity on MDA-MB-231 and MCF-7 cells under the TME conditions. In contrast, there was no obvious change in cell viability for the control groups (i.e., PBS, TME, GQDs), and GQDs-treated normal cell NIH-3T3 showed neglectable cytotoxicity (Supplementary Fig.12). The TME-responsive therapeutic effects of GQDs were further visualized by staining cells with propidium iodide (PI that stains dead cells) via time-lapse live-cell fluorescence imaging (Supplementary, movie 1&2). After the treatment with $100 \mu\text{g/ml}$ GQDs and $100 \mu\text{M H}_2\text{O}_2$, the number of 4T1 cells did no increase while the cancer cells in control group (PBS) grew remarkably over 24-h. Meanwhile, the red fluorescence signals of non-viable cells (PI dye) significantly increased during the 24-h treatment period, in comparison to the control groups. These results indicate that GQDs can efficiently interact with cancer cells and suppressed cell growth in the H_2O_2 -rich tumor microenvironment. Moreover, the anti-cancer efficiency of GQDs increased with increasing in the defect density of GQDs (Fig. 5b), consisting well with their defect-density-dependent catalytic activities (*vide supra*).

As a consequence, excessive ROS damages lipids, proteins, and DNA leading to cell death³⁶. To further investigate the anti-cancer mechanism of ROS generated from the GQDs-catalyzed H₂O₂ decomposition, we conducted comet assays to assess DNA damage. The round nuclear DNA without tails observed in the control groups indicates no obvious DNA damage, while the cells treated with GQDs under TME exhibited comet tails characteristic of DNA damage (Fig. 5c&d and Supplementary Fig. S14). Double-strand DNA breaks were revealed by a neutral comet assay (Fig. 5c). An average of 73% overall DNA damage was observed by alkaline comet assay (Fig. 5d). Therefore, the observed cell death could be attributed to the DNA damage-induced apoptosis caused by GQDs-catalyzed ROS generation. Mitochondria damage was also observed by measuring the mitochondrial membrane potential using lipophilic cationic dye JC-1³⁷. Specifically, JC-1 staining illustrated that mitochondrial potential was reduced after the GQDs treatment under TME (Fig. 5e), indicating significant mitochondria damage, which could also trigger the intrinsic apoptosis pathway^{2,38}. Also, it cannot be ruled out that necrosis could be triggered by the plasma membrane, a double layer of lipid and proteins, damage by the robust ROS level.

Cell death pathway. To investigate the cell death pathways, we employed annexin V-FITC/PI and flow cytometry to examine the effect of GQDs on cell necrosis and apoptosis. FITC conjugated Annexin V is typically used to detect apoptosis via binding to phosphatidylserine (PS), which is an early apoptosis marker that transports from the inner to the outer leaflet of the plasma membrane upon receiving pro-apoptotic signals³⁹⁻⁴⁰. PI acts as an impermeant cell dye that binds to DNA and stains cells with the broken cell membrane to indicate necrosis or late-stage apoptosis^{40,41}. As shown in Fig. 5f, GQDs therapeutic treatment in TME elicited remarkable necrosis (25.6%, Q1, PI+/Annexin V-) and significant apoptosis (17.8%, Q2 + Q4, the sum of PI-/Annexin V+ and PI+/Annexin V+) in 4T1 cells, compared to the controls (i.e. GQDs, TME) that showed neglectable necrosis and apoptosis. Notably, necrotic cell death is

closely associated with cell membrane rupture that is likely caused by the peroxidase-like activity of GQDs and ·OH-induced lipid peroxidation. Apoptosis could be ascribed to mitochondria damage and/or DNA damage, which is consistent with the ROS cancer inhibition mechanism discussed above.

Conclusions

In summary, we have demonstrated the ROS generation from H₂O₂ decomposition catalyzed by defect-rich metal-free GQDs and elucidated the associated anticancer mechanism. Defect-induced, GQDs-concentration-dependent, tumor microenvironment-selective cancer cell apoptosis was observed. Specifically, defect-rich GQDs exhibited high catalytic activities for the generation of abundant hydroxyl radicals from H₂O₂ decomposition in the tumor microenvironment, showing remarkable inhabitation effects toward cancer cells through multiple cellular component failures. Hydroxyl radicals thus produced caused DNA damage, interfered with mitochondria, and triggered subsequent apoptotic cell death pathways, while they could also damage the cell membrane, leading to cell necrosis. The demonstrated proof-of-concept and mechanistic understanding of the ROS generation from H₂O₂ decomposition catalyzed by defect-rich GQDs in the tumor microenvironment for cancer cell apoptosis/necrosis via DNA damage/cell membrane damage provide a promising strategy for the design and development of carbon catalyst-based safe and efficacious cancer therapy and other ROS-related biomedical applications.

Methods

Materials. Graphite rod (>99. 99999%), terephthalic acid (TA), 5,5-dimethyl-1-pyrroline-N-oxide (DMPO), 3,5,5-tetramethylbenzidine (TMB), hydrogen peroxide, cell count kit-8 (CCK-8), were purchased from Sigma. Dulbecco's Modified Eagle Medium (DMEM, #11995073), Gibco Roswell Park Memorial Institute- 1640 (RMPI 1640, #22400105) medium were purchased from ThermoFisher. Mili-Q water was used for synthesis and purification. Cell lines 4T1 (ATCCRL2541) and NIH 3T3 (#93061524) were obtained from American Type Culture Collection (ATCC) and CellBank Australia, respectively, they were both no mycoplasma contamination detected. MCF-7 and MDA-MB-231 cells were obtained from Sigma.

Synthesis of GQDs. GQDs were synthesized according to the published electrochemical method²⁶. Briefly, two graphite rods (>99.99999%, Sigma) as anode and cathode were inserted in ultrapure MiliQ water and subjected to 30V from a direct current power supply. After the electrochemical reaction for 120 h, a dark brown solution was obtained, from which GQDs were collected and purified via centrifugation at 10000rpm for 1 h, followed by filtration and freeze-drying.

Synthesis of GQDs-300 and GQDs-500. To produce GQDs-300 and GQDs-500, GQDs were treated at 300 °C and 500°C, respectively, for 30 min in the tube furnace with a ramp rate of 5°C/min under argon atmosphere.

Characterization of GQDs. HRTEM images were recorded on a JEOL-F200 scanning transmission electron microscope (S/TEM) equipped with a cold field emission gun and an EDS detector at an acceleration voltage of 200 kV. Raman spectra were recorded on a Renishaw InVia 2 Raman Microscope (532nm excitation, 1% laser power). X-ray photoelectron spectroscopy (XPS) was performed on a Thermo scientific ESCALAB250Xi spectrometer using a monochromatic Al K alpha X-ray source (energy 1486.68 eV) operated

at 120W (13.8 kV x 8.7 mA). Fourier-transform infrared spectroscopy was measured by Bruker compact FT-IR spectrometer ALPHA. Fluorescent emission spectroscopy was recorded on SHIMADZU RF-5301PC Spectrofluorophotometer. Ultraviolet photoelectron spectroscopy (UPS) data were obtained using the same instrument as XPS with a helium I ultraviolet source (energy 21.2eV). The hydrodynamic size distribution (DLS) and zeta potential were measured on Zetasizer Nanoseries (Malvern).

Catalytic performance evaluation. *Michaelis-Menten kinetics.* 3,3',5,5'-Tetramethylbenzene (TMB) was introduced to exam the catalytic performance and study the kinetic profiles, as the TMB undergoes a color oxidation reaction from colorless to blue to show absorption at 652nm, which was measured by UV-vis (JASCO V-770). The TMB concentration was calculated from absorbance via the Beer-Lambert law⁴²:

$$A = \varepsilon bc$$

where A is the absorbance, ε is the molar absorption coefficient of the oxidized TMB⁴³ ($39000\text{ M}^{-1}\text{cm}^{-1}$), b is the optical length (1cm), and c is the concentration of the oxidized TMB. Therefore, c was calculated by:

$$dc = \frac{dA}{\varepsilon b} = \frac{dA}{39000 \times 1} (\text{M})$$

The following condition was applied for relative activity test: TMB concentration: 800 $\mu\text{g}/\text{ml}$, Sample: 50 μL , H_2O_2 concentration: 1mM, at room temperature. Michaelis-Menten equation was selected as the model to analyze the enzyme kinetic⁴⁴.

$$V_0 = V_{max} \frac{[S]}{[S] + K_m}$$

The Michaelis-Menton constant (Km) and the maximum velocity (Vm) were achieved with the use of curve-fitting programs GraphPad Prism 9 software (the Michaelis- Menton curve fitting) 30,43.

Free radical identification. EPR signal was recorded on Bruker EMX X-Band EPR Spectrometer. In a typical experiment, DMPO (5 mM)⁴⁴ was added into the PBS buffer solution containing 50 µg/ml GQDs, to which 1 mM of H₂O₂ was added right before the measurements. The quantified analysis was performed using Xenon quantify EPR for peaks from 3450-3505 with the 2nd baseline correction⁴⁵. Radical concentrations were derived from the standard radical concentration curves, which were created based on the measurements of the ammonium iron sulfate Fe(NH₄)₂(SO₄)₂·6H₂O and hydrogen peroxide^{46,47}.

Cell culture. Breast cancer cell lines 4T1, MCF-7, MDA-MB-231, and fibroblast cell line NIH-3T3 were cultured in complete growth media (CGM) at 37 °C with 5% CO₂. CGM for MCF-7, MDA-MB-231, and NIH-3T3 cell lines are DMEM containing 10% fetal bovine serum (FBS) and 1% penicillin-streptomycin, i.e., penicillin 100 units/ml and streptomycin 100 µg/ml. CGM for the 4T1 cell line is RMPI-1640 containing 10% fetal bovine serum (FBS), and 1% penicillin-streptomycin. The cells were cultured at 37 °C in a humidified atmosphere with 5% CO₂ and passaged when reaching ATCC recommended confluency.

Cellular localization of GQDs. The cellular uptake biodistribution of GQDs was visualized by confocal microscopy. Briefly, coverslips were pre-disinfected and placed in a 24-well plate, followed by seeding 500 µl of MCF-7 cells in coverslip (1x10⁵ cells/ml). At 50% confluency, the CGM was removed, and cells were treated with PBS (control), TME (H₂O₂ 100 µM), and GQDs (100 µg/ml) only and GQDs (TME, H₂O₂ 100 µM) at 37 °C. After 24 h, the medium was removed, followed by rinsing with PBS three times. Cells were then stained with cell labels according to the manufacturer's instructions. Five µL Dil cell membrane dye (InvitrogenTM, V22885) and 995 µL serum-free medium were added into each well, incubated for 10 min at 37 °C. Dil membrane dye was then removed and cells were washed with PBS three times. Two drops of NucRed live 647 in 1 mL of fresh medium were added to each well. After 15 min

incubation at 37 °C, cells were fixed with 4% PFA and mounted with prolong diamond Antifade mountant and observed under the confocal microscope (Zeiss 780/900).

Intracellular ROS detection. Cell-permeable probe 2,7-Dichlorofluorescin diacetate (H₂DCFDA) was used to analyze the intracellular ROS generation via plate reader, confocal microscopy and flow cytometry. Briefly, 500 µl of 4T1 cells were seeded in a 24-well plate (1x10⁵ cells/ml). At 50% confluency, cells were washed with PBS three times and then incubated with DCFH-DA (10 µM) in serum-free RPMI 1640 for 30 min at 37 °C in the dark. Then the medium was removed, followed by rinsing with PBS three times. Cells were treated with PBS (control), TME (H₂O₂ 100 µM) and GQDs (100 µg/ml) only and GQDs (TME, H₂O₂ 100 µM). At 2h, 15h, 24h post-treatment, the DCF intensity was recorded on the plate reader (Molecular Device SpectraMax iD5).

To visualize the intracellular ROS level, 500 µl of 4T1 cells were seeded on the coverslip (1x10⁵ cells/ml). At 50% confluency, cells were washed with PBS three times then incubated with DCFH-DA (10 µM) in serum-free RPMI 1640 for 30mins at 37 °C in the dark. Then the medium was removed, followed by rinsing with PBS three times. Cells were treated with PBS (control), TME (H₂O₂ 100 µM) or GQDs (100 µg/ml) only, and GQDs (TME, H₂O₂ 100 µM) for 2-h incubation. Then, the cells were fixed with 4% PFA and mounted with Prolong diamond Antifade mountant for examination by confocal microscopy (Zeiss 780/900).

For flow cytometry analysis, 2 ml of 4T1 cells (3x10⁵ cells/ml) were seed into a 6-well plate. By following the same treatment procedure in the previous two experiments, cells were detached and collected, then measured immediately by flow cytometry (BD LSRFortessa) ($\lambda_{\text{excitation}} = 488\text{nm}$ and $\lambda_{\text{emission}} = 530\text{nm}$). The time course intensity measurements were carried out on a plate reader Molecular Device SpectraMax iD5, and the same seeding and treatments were applied to 4T1. After different periods, the plate was measured under excitation and emission at 488nm and 530nm, respectively.

Cell viability assay. CCK-8 assay was conducted to determine the in vitro cytotoxicity of GQDs. MCF-7/4T1/MDA-MB-231/3T3 cells were pre-incubated in a 96-well plate with a density of 5000 cells/well and cultured with 100 μ l complete growth medium for 24 h. Different concentrations of GQDs (0 to 1000 μ g/ml)/H₂O₂ (0 to 1000 μ M) were added and then incubated for 24h. After that, 10 μ l of CCk-8 reagent was added to each well and incubated for 4 h at 37 °C. The absorbance at 450 nm was measured using Molecular Device SpectraMax iD5. Data were presented as mean \pm SD from three independent experiments.

Apoptosis analysis. Cell Apoptosis was examined by annexin V/PI assay using Annexin V-FTIC apoptosis detection Kit (BNS500FI/100,eBioscience). 4T1 cells were pre-incubated in a 6-well plate at a density of 5000 cells/well and cultured with 2 ml of complete growth medium. At 50% confluence, cells were treated with PBS (control), TME (H₂O₂ 100 μ M), and GQDs (100 μ g/ml) only, and GQDs (TME, H₂O₂ 100 μ M). After 24 h incubation, cells were detached and collected using trypsin-EDTA (centrifugation at 190 g for 5 min). Cells were washed with PBS twice and binding buffer once (centrifugation at 200 g for 3 min), and then resuspended in binding buffer containing Annexin V-FTIC (5:200) and incubated for 10 min at room temperature. Cells were washed with binding buffer and stain with PI (10:200) in binding buffer. The flow cytometry (BD LSRFortessa) was used to measure the fluorescence of Annexin V - FITC and PI. All flow cytometry data were analyzed using Flowjo v10.

DNA damage Study

Comet assay

4T1/MCF-7/MDA-MB-231 cells were seeded in 6 wells plates (1x10⁵ cells/ml). At 50% confluence, complete growth media were replaced with the medium containing different treatment agents (i.e. the PBS, TME (H₂O₂ 100 μ M) or GQDs (100 μ g/ml) only, and GQDs (TME, H₂O₂ 100 μ M). After 24-h treatment, cells were detached with trypsin and resuspended

in ice-cold PBS (1×10^5 cells/ml), followed by cell lysis at 4 °C in dark for 2 h. Comet assay was then performed according to the protocol from the manufacturer. Briefly, 1% agarose gel was made by adding 1 g of agarose into 100ml MiliQ water using the microwave method, placed the gel in a 37°C water bath for at least 20 minutes to cool. Combine 1×10^5 /ml cell samples with agarose (at 37°C) at a ratio of 1:10 (v/v) and immediately pipette 50 µl onto Comet Slides. Slides were placed at 4°C in the dark for 30 minutes. Then Immersed slides in lysis Solution for 60 minutes. Drained excess buffer from slides and immerse in according electrophoresis buffer (TBE for Neutral Comet and AES for Alkaline Comet) for 20min. Then filled the horizontal electrophoresis cell (Bio-Rad) with electrophoresis buffers. The electrophoresis was conducted at 30V for 30 min under dark. Slides were gently removed from the electrophoresis tray and rinsed twice in Milli Q water and 70% ethanol⁴⁸⁻⁴⁹. Slides were dried and stained with SYBR Safe according to the manufacturer's instructions (1:10,000). Then, the images were captured using confocal microscopy (Zeiss 780/900). The results from comet assays were analyzed quantitatively by using ImageJ software by collectively monitoring more than 30 cells. % DNA in the tail was calculated using the following equation^{48,50}:

$$\%DNA\ in\ Tail = \left(1 - \frac{Total\ head\ DNA\ intensity}{Total\ DNA\ intensity} \right) \times 100\% \quad (\text{Error!} \\ \text{Bookmark} \\ \text{not} \\ \text{defined.2})$$

Neutral electrophoresis solution: TBE (obtained from UNSW store)

Alkaline electrophoresis solution (AES): 200 mM NaOH and 1 mM disodium EDTA pH >13

Mitochondria damage study. JC-1 (5,5',6,6'-tetrachloro-1,1'3,3'-tetraethyl-imidacarbocyanine iodide, Abcam) was applied to measure membrane potential change of

mitochondria. 4T1 cells were cultured in a 96-well plate (Corning) at a density of 5000 cells/well, at 50% confluence, the complete growth media were replaced with media containing different treatments (control (PBS), TME, GQDs (100ug/ml), GQD (TME)) after 24 h incubation. Then, cells were washed with JC-1 dilution buffer containing 10% FBS and stained with JC-1 working solution (100 µl, 1 µM) in the dark for 15min. Thereafter, cells were washed with JC-1 dilution buffer twice and then emissions were recorded using Molecular Device SpectraMax iD5 (red: excitation: 530 nm, emission: 590 nm; green: excitation: 475 nm, emission: 530 nm).

Data availability

All data in the published article or supplementary files are available on request from the authors.

Acknowledgments

The authors greatly acknowledge the financial support from ARC Discovery Projects (DP200103587). The authors acknowledge the use of facilities in the Electron Microscope Unit, Solid State & Elemental Analysis Unit, Spectroscopy Laboratory, NMR Facility, Biomedical Imaging Facility and Flow Cytometry Facility within the Mark Wainwright Analytical Centre (MWAC) at UNSW Sydney. The authors thank Dr.Chenhao Zhang for the assistance with the operation of the Electron Microscope.

Funding

The authors greatly acknowledge the financial support from ARC Discovery Projects (DP200103587).

Author information

Affiliations

Australian Carbon Materials Centre (A-CMC), School of Chemical Engineering, University of New South Wales, Sydney, NSW, 2052, Australia.

Xichu Wang, [@xichu.wang@unsw.edu.au.](mailto:@xichu.wang@unsw.edu.au)

Chuangang Hu, [@chuangang.hu@unsw.edu.au.](mailto:@chuangang.hu@unsw.edu.au)

Zi Gu, [@zi.gu1@unsw.edu.au.](mailto:@zi.gu1@unsw.edu.au)

Liming Dai, [@l.dai@unsw.edu.au.](mailto:@l.dai@unsw.edu.au)

Author contributions

The author contributions for this work are as follows: conceptualization: Z.G. and L.D. Data collections: X.W. Formal analysis and investigation: X.W and C.H. Writing the original draft: X.W, Z.G., and L.D. Funding acquisition: Z.G. and L.D. Supervision and validation: Z.G. and L.D.

Corresponding authors

Correspondence to Zi Gu and Liming Dai.

Ethics declaration

Ethic approval and consent to participate

Not applicable

Consent for publication

Not applicable

Conflict of Interest

The authors declare no conflict of interest.

References

1. Kim, J. Y. & Park, J. H. ROS-dependent caspase-9 activation in hypoxic cell death. *FEBS Lett.* **549**, 94–98 (2003).
2. Radogna, F. *et al.* Cell type-dependent ROS and mitophagy response leads to apoptosis or necroptosis in neuroblastoma. *Oncogene* **35**, 3839–3853 (2016).
3. Fan, J. *et al.* Bruceine D induces lung cancer cell apoptosis and autophagy via the ROS/MAPK signaling pathway in vitro and in vivo. *Cell Death Disease*. **11**, (2020).
4. Du, X. *et al.* Acetoacetate induces hepatocytes apoptosis by the ROS-mediated MAPKs pathway in ketotic cows. *J. Cell. Physiology*. **232**, 3296–3308 (2017).
5. Sharma, V., Anderson, D. & Dhawan, A. Zinc oxide nanoparticles induce oxidative DNA damage and ROS-triggered mitochondria mediated apoptosis in human liver cells (HepG2). *Apoptosis* **17**, 852–870 (2012).
6. Saleem, J., Wang, L. & Chen, C. Carbon-Based Nanomaterials for Cancer Therapy via Targeting Tumor Microenvironment. *Adv. Healthcare Mater.* **7**, 1–30 (2018).
7. López-Lázaro, M. Dual role of hydrogen peroxide in cancer: Possible relevance to cancer chemoprevention and therapy. *Cancer Lett.* **252**, 1–8 (2007).
8. Gao, L. *et al.* Intrinsic peroxidase-like activity of ferromagnetic nanoparticles. *Nat.*

Nanotechnol. **2**, 577–583 (2007).

9. Pan, X. *et al.* Metal–organic-framework-derived carbon nanostructure augmented sonodynamic cancer therapy. *Adv. Mater.* **30**, 1–9 (2018).
10. Yu, L., Hu, P. & Chen, Y. Gas-generating nanoplatforms: Material chemistry, multifunctionality, and gas therapy. *Adv. Mater.* **30**, 1–40 (2018).
11. Zhu, H. *et al.* Cobalt nanowire-based multifunctional platform for targeted chemo-photothermal synergistic cancer therapy. *Colloids Surfaces B Biointerfaces* **180**, 401–410 (2019).
12. Nappi, A. J. & Vass, E. Hydroxyl radical production by ascorbate and hydrogen peroxide. *Neurotox. Res.* **2**, 343–355 (2000).
13. Qin, Q., Liu, Y., Li, X., Sun, T. & Xu, Y. Enhanced heterogeneous Fenton-like degradation of methylene blue by reduced CuFe₂O₄. *RSC Adv.* **8**, 1071–1077 (2018).
14. Liu, X. & Dai, L. Carbon-based metal-free catalysts. *Nat. Rev. Mater.* **1**, (2016).
15. Gong, Kuanping, Feng Du, Dai, Zhenhai Xia, L. Nitrogen-doped carbon nanotube arrays with high electrocatalytic activity for oxygen reduction. *Science* **323**, 760–764 (2009).
16. Dai, L. *Carbon-Based Metal-Free Catalysts:Design and Applications*. Wiley-VCH vol. 1 (Wiley-VCH Verlag GmbH & Co. KGaA, 2018).
17. Fan, K. *et al.* In vivo guiding nitrogen-doped carbon nanozyme for tumor catalytic therapy. *Nat. Commun.* **9**, (2018).
18. Hu, C. & Dai, L. Doping of carbon materials for metal-free electrocatalysis. *Adv. Mater.* **31**, 1–17 (2019).
19. Yan, D. *et al.* Defect chemistry of nonprecious-metal electrocatalysts for oxygen reactions. *Adv. Mater.* **29**, 1–20 (2017).
20. Zhang, L., Xu, Q., Niu, J. & Xia, Z. Role of lattice defects in catalytic activities of graphene clusters for fuel cells. *Phys. Chem. Chem. Phys.* **17**, 16733–16743 (2015).
21. Jiang, Y. *et al.* Significant contribution of intrinsic carbon defects to oxygen reduction activity. *ACS Catal.* **5**, 6707–6712 (2015).
22. Hu, C. *et al.* Carbon Nanomaterials for energy and biorelated catalysis : Recent advances and looking forward. *ACS Cent. Sci.* **5**, 389–408 (2019).

23. Varghese, N. *et al.* Binding of DNA nucleobases and nucleosides with graphene. *ChemPhysChem* **10**, 206–210 (2009).
24. Lei Qi, Tonghe Pan, Liling Ou, Zhiqiang Ye, Chunlei Yu, Bijun Bao, Zixia Wu, Dayong Cao, L. D. Biocompatible nucleus-targeted graphene quantum dots for selective killing of cancer cells via DNA damage. *Nat. Commun. biology* **4**, 1-12. (2021).
25. Liu, Y. *et al.* Efficient synthesis and physical properties of novel H-shaped 2,3,7,8-tetraazaanthracene-based conjugated molecules. *Chem. Commun.* **48**, 4166–4168 (2012).
26. Liu, J. *et al.* Metal-free efficient photocatalyst for stable visible water splitting via a two-electron pathway. *Science*. **347**, 970–974 (2015).
27. Li, S. *et al.* Targeted tumour theranostics in mice via carbon quantum dots structurally mimicking large amino acids. *Nat. Biomed. Eng.* (2020)
28. Jia, Y., Chen, J. & Yao, X. Defect electrocatalytic mechanism: Concept, topological structure and perspective. *Mater. Chem. Front.* **2**, 1250–1268 (2018).
29. Leonat, L., Sbârcea, G. & Brañzoi, I. V. Cyclic voltammetry for energy levels estimation of organic materials. *UPB Sci. Bull. Ser. B Chem. Mater. Sci.* **75**, 111–118 (2013).
30. Cao, Z. *et al.* Biodegradable 2D Fe–Al Hydroxide for Nanocatalytic tumor-dynamic therapy with tumor specificity. *Adv. Sci.* **5**, (2018).
31. Gonzalez, D. H., Kuang, X. M., Scott, J. A., Rocha, G. O. & Paulson, S. E. Terephthalate probe for hydroxyl radicals: Yield of 2-hydroxyterephthalic acid and transition metal interference. *Anal. Lett.* **51**, 2488–2497 (2018).
32. Sun, H., Gao, N., Dong, K., Ren, J. & Qu, X. Graphene quantum dots-band-aids used for wound disinfection. *ACS Nano* **8**, 6202–6210 (2014).
33. Yang, B., Ding, L., Yao, H., Chen, Y. & Shi, J. A Metal-organic framework (MOF) Fenton nanoagent-enabled nanocatalytic cancer therapy in synergy with autophagy inhibition. *Adv. Mater.* **32**, 1–12 (2020).
34. Balaraman Kalyanaraman, Victor Darley-Usmar, K. J. A. D. Measuring reactive oxygen and nitrogen species with fluorescent probes: challenges and limitations. *Bone* **23**, 1–7 (2008).
35. Hao, G., Xu, Z. P. & Li, L. Manipulating extracellular tumour pH: An effective target

for cancer therapy. *RSC Adv.* **8**, 22182–22192 (2018).

36. Phaniendra, A., Jestadi, D. B. & Periyasamy, L. Free Radicals: Properties, sources, targets, and their implication in various diseases. *Indian J. Clin. Biochem.* **30**, 11–26 (2015).
37. Elefantova, K., Lakatos, B., Kubickova, J., Sulova, Z. & Breier, A. Detection of the mitochondrial membrane potential by the cationic dye JC-1 in l1210 cells with massive overexpression of the plasma membrane ABCB1 drug transporter. *Int. J. Mol. Sci.* **19**, 1–14 (2018).
38. Yee, C., Yang, W. & Hekimi, S. The intrinsic apoptosis pathway mediates the pro-longevity response to mitochondrial ROS in *C elegans*. *Cell* **157**, 897–909 (2014).
39. Fadeel, B. & Xue, Di. The ins and outs of phospholipid asymmetry in the plasma membrane: roles in health and disease. *Crit Rev Biochem Mol Biol* **44**, 264–277 (2009).
40. Logue, S. E., Elgendi, M. & Martin, S. J. Expression, purification and use of recombinant annexin V for the detection of apoptotic cells. *Nat. Protoc.* **4**, 1383–1395 (2009).
41. Hu, K. *et al.* Marriage of black phosphorus and Cu²⁺ as effective photothermal agents for PET-guided combination cancer therapy. *Nat. Commun.* **11**, 1–15 (2020).
42. Spectronic, T. Basic UV-Vis Theory , Concepts and Applications Basic UV-Vis Theory , Concepts and Applications. 1–28.
43. Song, Y., Qu, K., Zhao, C., Ren, J. & Qu, X. Graphene oxide: Intrinsic peroxidase catalytic activity and its application to glucose detection. *Adv. Mater.* **22**, 2206–2210 (2010).
44. Cornish-Bowden, A. One hundred years of Michaelis–Menten kinetics. *Perspect. Sci.* **4**, 3–9 (2015).
45. Clément, J. L. *et al.* Assignment of the EPR spectrum of 5,5-dimethyl-1-pyrroline N-oxide (DMPO) superoxide spin adduct. *J. Org. Chem.* **70**, 1198–1203 (2005).
46. Weber, R. T. Xenon Data Processing Reference. *Bruker*. (2012).
47. Tada, M., Kohno, M. & Niwano, Y. Alleviation effect of arbutin on oxidative stress generated through tyrosinase reaction with L-tyrosine and L-DOPA. *BMC Biochem.* **15**, 1–7 (2014).

48. Collins, A. R. The comet assay for DNA damage and repair: Principles, applications, and limitations. *Appl. Biochem. Biotechnol. - Part B Mol. Biotechnol.* **26**, 249–261 (2004).
49. Olive, P. L. & Banáth, J. P. The comet assay: A method to measure DNA damage in individual cells. *Nat. Protoc.* **1**, 23–29 (2006).
50. Lu, Y., Liu, Y. & Yang, C. Evaluating in vitro DNA damage using comet assay. *J. Vis. Exp.* **2017**, 2–7 (2017).

Supplementary Files

This is a list of supplementary files associated with this preprint. Click to download.

- [graphicabstract.docx](#)
- [SIXichudefectrichGQD.pdf](#)
- [Supplementaryvideo1livecellimagewithGQDs treatment.gif](#)
- [Supplementaryvideo2LivecellimagePIGQDs4T1cells.gif](#)
- [Supplementaryvideo3cellularuptake.gif](#)
- [Supplementaryvideo43Dcellularuptake.gif](#)